Trem2-expressing multinucleated giant macrophages are a biomarker of good prognosis in head and neck squamous cell carcinoma

Grégoire Gessain, Ahmed-Amine Anzali, Marvin Lerousseau, Kevin Mulder, Mathilde Bied, Anne Auperin, Daniel Stockholm, Nicolas Signolle, Farah Sassi, Maria Eugenia Marques da Costa, et al.

▶ To cite this version:

Grégoire Gessain, Ahmed-Amine Anzali, Marvin Lerousseau, Kevin Mulder, Mathilde Bied, et al.. Trem2-expressing multinucleated giant macrophages are a biomarker of good prognosis in head and neck squamous cell carcinoma. Cancer Discovery, 2024, 14 (12), pp.2352-2366. 10.1158/2159-8290.CD-24-0018 . inserm-04729854

HAL Id: inserm-04729854

https://inserm.hal.science/inserm-04729854v1

Submitted on 10 Oct 2024

RESEARCH BRIEF

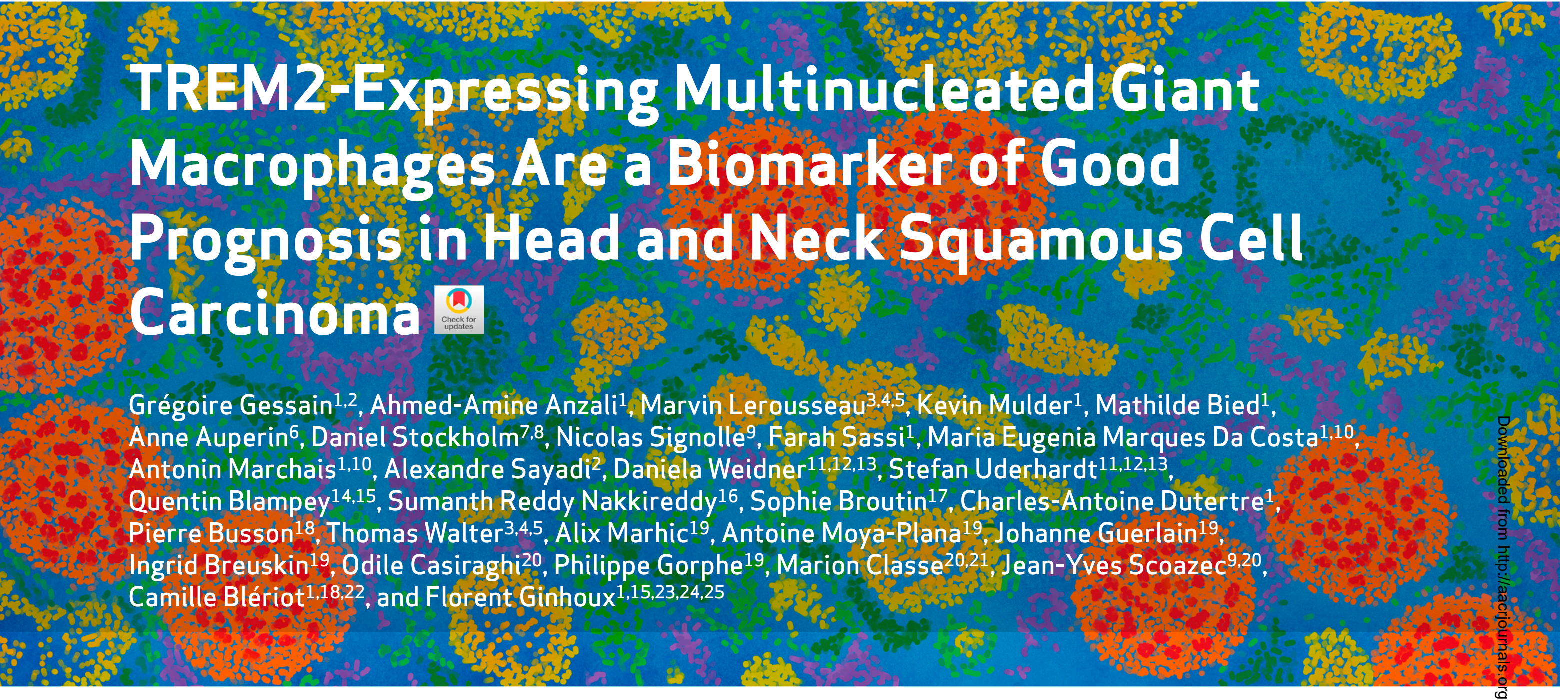

TREM2-Expressing Multinucleated Giant Macrophages Are a Biomarker of Good Prognosis in Head and Neck Squamous Cell Carcinoma

Grégoire Gessain[1,2], Ahmed-Amine Anzali[1], Marvin Lerousseau[3,4,5], Kevin Mulder[1], Mathilde Bied[1], Anne Auperin[6], Daniel Stockholm[7,8], Nicolas Signolle[9], Farah Sassi[1], Maria Eugenia Marques Da Costa[1,10], Antonin Marchais[1,10], Alexandre Sayadi[2], Daniela Weidner[11,12,13], Stefan Uderhardt[11,12,13], Quentin Blampey[14,15], Sumanth Reddy Nakkireddy[16], Sophie Broutin[17], Charles-Antoine Dutertre[1], Pierre Busson[18], Thomas Walter[3,4,5], Alix Marhic[19], Antoine Moya-Plana[19], Johanne Guerlain[19], Ingrid Breuskin[19], Odile Casiraghi[20], Philippe Gorphe[19], Marion Classe[20,21], Jean-Yves Scoazec[9,20], Camille Blériot[1,18,22], and Florent Ginhoux[1,15,23,24,25]

ABSTRACT

Patients with head and neck squamous cell carcinomas (HNSCC) often have poor outcomes due to suboptimal risk management and treatment strategies; yet integrating novel prognostic biomarkers into clinical practice is challenging. Here, we report the presence of multinucleated giant cells (MGC)—a type of macrophages—in tumors from patients with HNSCC, which are associated with a favorable prognosis in treatment-naive and preoperative chemotherapy–treated patients. Importantly, MGC density increased in tumors following preoperative therapy, suggesting a role of these cells in the antitumoral response. To enable clinical translation of MGC density as a prognostic marker, we developed a deep-learning model to automate its quantification on routinely stained pathological whole slide images. Finally, we used spatial transcriptomic and proteomic approaches to describe the MGC-related tumor microenvironment and observed an increase in central memory CD4 T cells. We defined an MGC-specific signature resembling to TREM2-expressing mononuclear tumor-associated macrophages, which colocalized in keratin tumor niches.

SIGNIFICANCE: Novel individual biomarkers are needed to guide therapeutic decisions for patients with head and neck cancer. We report for the first time, granulomas of TREM2-expressing multinucleated giant macrophages in keratin-rich tumor niches, as a biomarker of favorable prognosis and developed a deep-learning model to automate its quantification on routinely stained pathological slides.

---

[1] INSERM U1015, Gustave Roussy Cancer Campus, Bâtiment de Médecine Moléculaire, Villejuif, France. [2] Université Paris Cité, Faculté de Santé, Paris, France. [3] Center for computational biology (CBIO), Mines Paris, PSL University, Paris, France. [4] Institut Curie, PSL University, Paris, France. [5] INSERM, U900, Paris, France. [6] Biostatistics and Epidemiology Office, Gustave Roussy, Oncostat INSERM 1018, Labelled Ligue Contre le Cancer, Université Paris-Saclay, Villejuif, France. [7] PSL Research University, EPHE, Paris, France. [8] Sorbonne Université, INSERM, Centre de Recherche Saint-Antoine, CRSA, Paris, France. [9] Experimental and Translational Pathology Platform, AMMICa, INSERM US23/UAR3655, Gustave Roussy, Villejuif, France. [10] Department of Pediatric and Adolescent Oncology, Gustave Roussy Cancer Campus, Université Paris-Saclay Villejuif, France. [11] Department of Internal Medicine 3-Rheumatology and Immunology, Friedrich-Alexander-University Erlangen-Nürnberg (FAU) and Universitätsklinikum Erlangen, Erlangen, Germany. [12] Deutsches Zentrum für Immuntherapie (DZI), Friedrich-Alexander-University Erlangen-Nürnberg (FAU) and Universitätsklinikum Erlangen, Erlangen, Germany. [13] Exploratory Research Unit, Optical Imaging Centre Erlangen, Friedrich-Alexander-University Erlangen-Nürnberg (FAU), Erlangen, Germany. [14] Paris-Saclay University, CentraleSupélec, laboratory of Mathematics and Computer Science (MICS), Gif-sur-Yvette, France. [15] Paris-Saclay University, Gustave Roussy, Villejuif, France. [16] Department of Artificial Intelligence and Informatics Research, Mayo Clinic, Jacksonville, Florida. [17] Department of Pharmacology, Institut Gustave Roussy, Villejuif, France. [18] CNRS, UMR 9018, Gustave Roussy and Université Paris-Saclay, 39, rue Camille Desmoulins, Villejuif, France. [19] Department of Head and Neck Oncology, Gustave Roussy Cancer Campus Villejuif, France. [20] Department of Pathology, University Paris-Saclay, Gustave Roussy Cancer Center, Villejuif, France. [21] Precision Medicine and Computational Biology, Sanofi Research France, Paris, France. [22] Institut Necker Enfants Malades (INEM), CNRS

INTRODUCTION

Squamous cell carcinoma (SCC) is one of the most frequent carcinomas and arises in several organs including lung, head and neck, esophagus, skin, and uterine cervix. Among these, head and neck SCC (HNSCC) is particularly common, with 890,000 new cases and 450,000 deaths globally in 2020. Its incidence is rising, expected to escalate by 20% by 2030, representing 1.08 millions of new cases per year (1). Current treatments include surgery, chemotherapy, and radiotherapy; alongside, immunotherapy is now approved for recurrent, metastatic, and unresectable carcinomas (2). However, more than 50% of patients experience recurrent or metastatic disease within 3 years of diagnosis (2) often facing numerous complications or disabilities even after recovery (3). Gold standard patient stratification is the tumor–node–metastasis staging where patients with equivalent staging receive similar treatment although they often hold heterogeneous outcomes. Such suboptimal stratification led to inadequate therapy with undertreatment compromising patient recovery or overtreatment increasing adverse events and unnecessary costs. Therefore, there is an unmet clinical need for novel individual prognostic biomarkers to guide therapeutic decisions.

A deeper understanding of cancer biology is essential for improving treatment. Recent studies have underscored the long under-appreciated role of the tumor microenvironment (TME) in shaping all stages of the disease (4). Within the TME, tumor-associated macrophages (TAM) are particularly abundant and influential (5). Recent single-cell RNA sequencing (scRNAseq) studies have described several conserved TAM transcriptional programs across tumors (6). Of particular interest, macrophages expressing the Triggering Receptor Expressed on Myeloid Cells-2 (TREM2) have been shown to exert immunosuppressive and protumoral functions in various cancers (7, 8).

Alongside conventional TAMs, a proportion of HNSCC also contains macrophages that exhibit a large cytoplasm and multiple nuclei, termed multinucleated giant cells (MGC; ref. 9). In SCC, macrophages and monocytes fuse to form MGC, performing a “foreign body reaction” against extracellular keratin produced by carcinomatous cells (9). While their presence is well documented in keratinizing SCC (10), their biology is not well understood in tumors and studies suggest varying impact of MGC on patient survival in esophageal and oral SCC (11–13). Conventional methods such as flow cytometry and scRNAseq struggle to analyze these cells due to their extraordinary size, leaving their clinical impact in SCC largely unexplored.

Herein, we used samples from several large cohorts of patients with HNSCC to ask about the association between MGC and survival following resection of their tumors. We investigated the interaction between chemotherapy, MGC, and patient outcomes and devised a methodology for clinical use adaptable to various SCC. Additionally, we employed spatial transcriptomic and proteomic approaches on tumor microscopic slides to dive further into the MGC-related TME and reveal the unique scRNA signature of MGC within keratin-rich tumor niches and their possible relationship to TREM2-expressing TAM.

RESULTS

MGC Are a Biomarker of Good Prognosis in Patients with HNSCC

We first characterized the presence and abundance of MGC in tumors from patients with HNSCC who underwent primary surgery (Fig. 1A). We used cohorts from The Cancer Genome Atlas (TCGA) and Gustave Roussy (GR; refs. 14, 15), consisting of 394 patients with oral cavity (Fig. 1B). We observed that 292 patients bore keratinizing tumors, while the remaining 102 did not (Fig. 1C and D). Within keratinizing tumors, we observed MGC that were aggregated in large granulomatous clusters in close contact with extracellular keratin (Fig. 1E). Interestingly, none of the non-keratinizing tumors contained MGC, while 33% of highly keratinizing tumors contained high MGC densities (Fig. 1F). Although MGC abundance was significantly associated with the keratinization level of the tumors, the presence of keratin did not guarantee the presence of MGC as 37% of patients with highly keratinizing SCC were devoid of MGC infiltration (Supplementary Fig. S1A and S1B).

We then asked whether the density of MGC in these tumors was related to patient outcomes. Using microscopic slides of HNSCC cohorts from TCGA ($n = 110$ patients) and from GR ($n = 284$ patients), we stratified patients into three groups ($\mathrm{MGC}^{\mathrm{High}}$, $\mathrm{MGC}^{\mathrm{Int}}$, and $\mathrm{MGC}^{\mathrm{Low}}$) according to the MGC density in their tumor (Supplementary Fig. S1C and S1D; Supplementary Table S1). In both cohorts, we saw that higher densities of MGC were associated with longer overall survival (OS; Fig. 1G and H) and progression-free interval (PFI; Supplementary Fig. S1E and S1F). In the combined TCGA and GR cohorts ($n = 394$ patients), we observed a positive association between MGC density and OS and PFI with a linear relationship between log-hazard of death and MGC density and the square root of MGC density and between log-hazard of event and the square root of MGC density (Supplementary Fig. S1G and S1H; Supplementary Tables S2–S4). A significant association was also observed when MGC density was categorized in the three groups ($\mathrm{MGC}^{\mathrm{High}}$, $\mathrm{MGC}^{\mathrm{Int}}$, and $\mathrm{MGC}^{\mathrm{Low}}$; Fig. 1I and J). Demographic and disease characteristics of the patients were well balanced between the three groups (Supplementary Table S2). In multivariate analyses adjusted for sex, age, p-stage, location, tobacco, and alcohol consumption, the density of MGC in the tumor (whether in three categories

---

UMR 8253, INSERM U1151, Paris, France. [23]Department of Immunology and Microbiology, Shanghai Institute of Immunology, Shanghai Jiao Tong University School of Medicine, Shanghai, China. [24]Singapore Immunology Network (SIgN), A*STAR, Singapore, Singapore. [25]Translational Immunology Institute, SingHealth/Duke-NUS Academic Medical Centre, Singapore, Singapore.

Corresponding Author: Florent Ginhoux, Bâtiment de Médecine Moléculaire, 114 rue Edouard Vaillant, Villejuif 94800, France. E-mail: florent.ginhoux@gustaveroussy.fr

Cancer Discov 2024;14:2352–66

doi: 10.1158/2159-8290.CD-24-0018

or with the square root of density as a continuous variable) was significantly associated with OS and PFI (Supplementary Tables S3 and S4). Importantly, high keratinization in the context of low/intermediate MGC densities was not associated with a better OS and PFI (Supplementary Fig. S1I–S1K; Supplementary Table S5), showing that it is not high keratinization *per se* that correlates with outcome.

In addition, we asked whether tumor-infiltrating lymphocytes (TILs) density, tumor grade, and CD68-positive mononuclear macrophages were related to the prognosis value of MGC. $\mathrm{MGC}^{\mathrm{High}}$ patients had higher levels of TILs as compared to $\mathrm{MGC}^{\mathrm{Int}}$ and $\mathrm{MGC}^{\mathrm{Low}}$ patients (Supplementary Fig. S2A–S2C) and in univariate analysis, TILs were significantly associated with OS (P value = 0.0002) and PFI (P value = 0.0008; Supplementary Tables S6 and S7). In addition, higher tumor grade was associated with higher risk of death and events (Supplementary Fig. S2D and S2E; Supplementary Tables S6 and S7). Importantly, in multivariate analysis adjusted for TILs and tumor grade, MGC remained significantly associated with survival and PFI (Supplementary Tables S3 and S4). Finally, CD68 mononuclear macrophages did not show significant association with risk of death and events (Supplementary Fig. S2F and S2G; Supplementary Tables S6 and S7).

Taken together, these data show that patients with HNSCC bearing keratinizing tumors are more likely to have positive outcomes in the presence of high MGC densities.

Induction-Chemotherapy Induces MGC Formation

Next, we extended our investigation to include a cohort of patients with HNSCC (n = 52 patients) treated by three cycles of induction-chemotherapy (ICT) followed by surgery and adjuvant therapy (Fig. 1K and L). Patients were classified into three groups: no residual tumor and residual tumors having either high ($\mathrm{MGC}^{\mathrm{High}}$) or low/intermediate ($\mathrm{MGC}^{\mathrm{Low/Int}}$) MGC densities (Fig. 1L and M; Supplementary Fig. S3A and S3B). Interestingly, high MGC densities in surgical resections were more common after ICT compared to treatment-naive patients (Fig. 1N), suggesting that ICT might induce the formation of MGC. As observed in treatment-naive patients, higher MGC densities associated with longer OS, comparable to patients with no residual tumor (Fig. 1O). Pathological response was similarly correlated with MGC density: good/partial responders had higher MGC densities than poor responders (Fig. 1P).

In summary, MGC density is associated with good outcome in patients with HNSCC either in the presence or absence of ICT prior to surgical resection.

Automatic Detection of MGC and Tumor Cells on H&E/HES WSI by Deep Learning

Effective stratification of patients with cancer is a mainstay of good clinical management, yet few novel biomarkers prove amenable to quick and easy measurement in hospital routine: for example, here, it would take a trained pathologist up to 30 minutes per slide to assess MGC density. Therefore, we aimed to establish a high-throughput automatic method to detect and enumerate MGC and compute the biomarker on whole-slide images (WSI) of patients with SCC. We trained two models on routinely hematoxylin and eosin (H&E)/hematoxylin, eosin, saffron (HES) stained WSI: one that detects tumor cells and one that detects MGC (Fig. 2A and B). More than 5,000 manually annotated MGC and more than 800,000 manually annotated carcinomatous cells from the TCGA and GR cohorts were used to train the MGC and tumor cells detection model. The automated biomarker was computed as the total number of detected MGC divided by the total number of detected tumor cells, across all available slides for each patient.

After training, we validated the performance of both detection models on 110 slides from TCGA cohort and 839 slides from GR cohort. Slides from the GR cohort used for training were excluded from the validation cohort. We found that the models performed comparably to pathologists, both for MGC in TCGA (average precision (AP) = 0.8188) and GR (AP = 0.7524) as well as for tumor cells in TCGA (AP = 0.688) and GR (AP = 0.679) cohorts. Additionally, the MGC detection model performed comparably to pathologists at the slide-level in TCGA ($r^2 = 0.8792$; $P < 0.0001$) and GR cohorts ($r^2 = 0.7811$; $P < 0.0001$; Fig. 2C–F). We then assessed the performance of the artificial intelligence (AI) versus the manual biomarker. On the 949 slides (representing 341 patients) that passed quality control (Supplementary Fig. S4A), the automatic MGC biomarker correlated with the manual MGC density in TCGA ($r^2 = 0.7833$; $P < 0.0001$) and GR ($r^2 = 0.4036$; $P < 0.0001$; Supplementary Fig. S4B and S4C) cohorts. When comparing the ranking of the predicted patient AI scores with the manually computed groups, the AI obtained a

Figure 1. MGC density is a biomarker of prognosis in patients with HNSCC. **A,** Therapeutic sequence of the treatment-naive cohorts of patients with HNSCC from TCGA and GR. **B,** Flow chart of TCGA and GR cohorts of treatment-naive patients with HNSCC. Among the 946 patients (527 from TCGA and 419 from GR), 394 were included (110 from TCGA and 284 from GR). **C,** Non-keratinizing HNSCC (left) and keratinizing HNSCC (right), stained by H&E. WSI from TCGA (scale bar, 250 μm). **D,** Histograms showing the number of $\mathrm{K}^{\mathrm{Low}}$ and $\mathrm{K}^{\mathrm{High}}$ patients from TCGA and GR. **E,** Keratinizing SCC of the oral cavity of a patient from GR, with MGC-rich granulomas surrounding keratin debris. Left, low magnification of the carcinoma (scale bar, 2 mm). Middle, high magnification of a granuloma containing MGC and keratin (scale bar, 50 μm). Right, MGC are highlighted in yellow and keratin in red. **F,** Histograms showing the proportion of $\mathrm{MGC}^{\mathrm{high}}$ patients (TCGA and GR cohorts) among the keratinization groups (no, low, moderate, and high). **G,** OS curve of 110 TCGA patients stratified according to MGC density in their tumors. The vertical tick mark on the curves means that a patient was censored at this time. **H,** OS curve of 284 GR patients stratified according to MGC density in their tumors. **I,** OS curve of all patients (TCGA and GR) stratified according to MGC density in their tumors. **J,** PFI curve of all patients (TCGA and GR) stratified according to MGC density in their tumors. **K,** Therapeutic sequence of the induction chemotherapy (ICT)-treated cohort of patients with HNSCC from GR. **L,** Flow chart of the ICT-treated cohort of patients with HNSCC from GR. **M,** Keratinizing oral SCC from a patient treated at GR whose tumor responded well to ICT, showing areas of keratin surrounded by numerous MGC. Left, low magnification of the carcinoma (scale bar, 2 mm). Middle, high magnification of a granuloma containing MGC and keratin (scale bar, 50 μm). Right, MGC are highlighted in yellow and keratin in red. **N,** Histograms showing the percentage of patients with no residual tumor, and the percentage of patients with residual tumor being $\mathrm{MGC}^{\mathrm{High}}$ or $\mathrm{MGC}^{\mathrm{Low/Int}}$, in treatment-naive (TCGA and GR) and ICT patients (GR). **O,** OS curve of 52 patients treated by ICT at GR, stratified by their tumor content and MGC density on surgical resection. The vertical tick mark on the curves means that a patient was censored at this time. **P,** Histograms showing the proportion of $\mathrm{MGC}^{\mathrm{High}}$ and $\mathrm{MGC}^{\mathrm{Low/Int}}$ patients according to the pathological response status of their tumors (poor vs. good/partial).

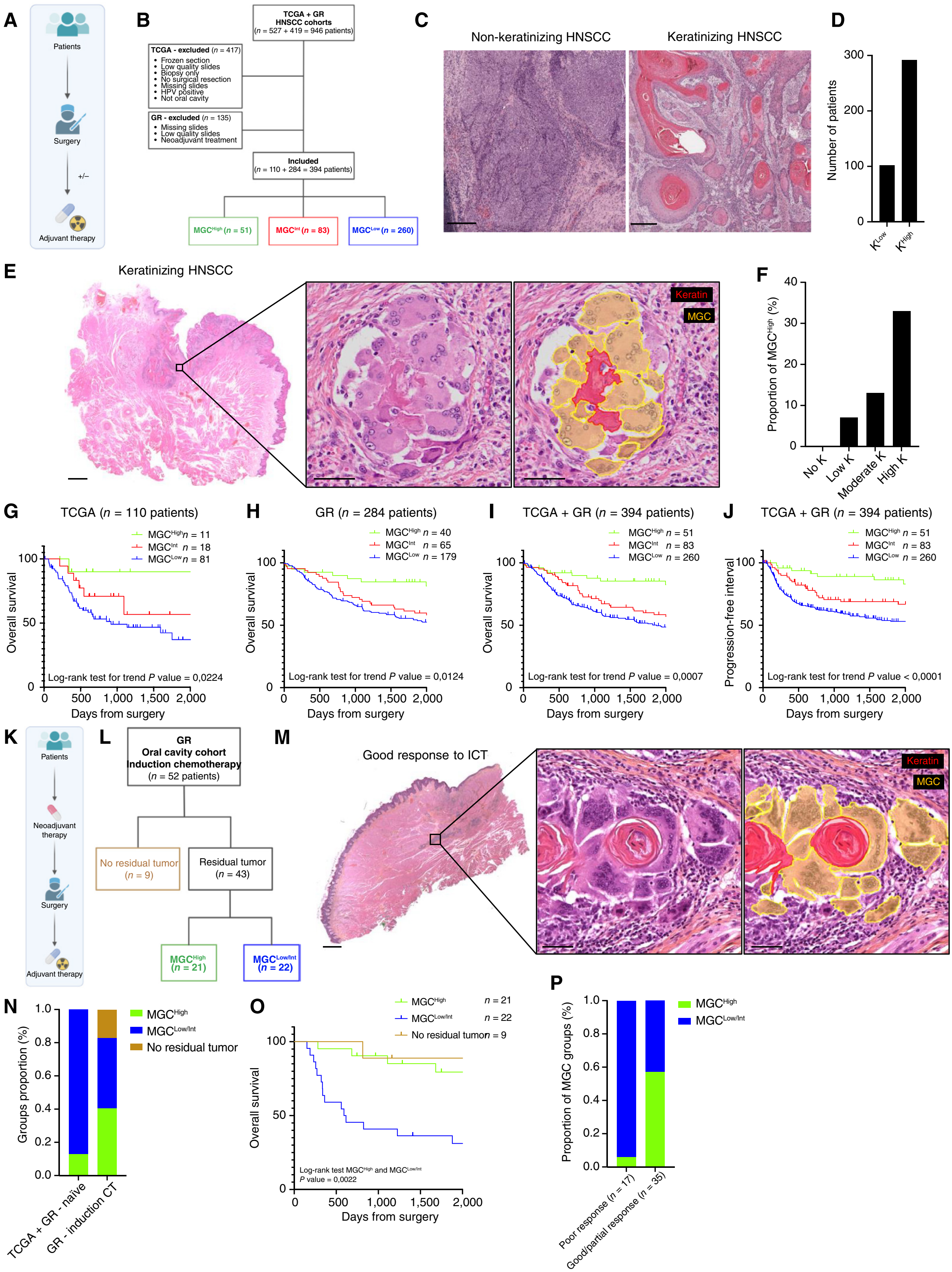
A
Patients
Surgery
+/–
Adjuvant therapy
B
TCGA + GR
HNSCC cohorts
(n = 527 + 419 = 946 patients)
TCGA - excluded (n = 417)
• Frozen section
• Low quality slides
• Biopsy only
• No surgical resection
• Missing slides
• HPV positive
• Not oral cavity
GR - excluded (n = 135)
• Missing slides
• Low quality slides
• Neoadjuvant treatment
Included
(n = 110 + 284 = 394 patients)
MGC^High (n = 51)
MGC^Int (n = 83)
MGC^Low (n = 260)
C
Non-keratinizing HNSCC
Keratinizing HNSCC
D
Number of patients
0
100
200
300
K^Low
K^High
E
Keratinizing HNSCC
Keratin
MGC
F
Proportion of MGC^High (%)
0
10
20
30
40
No K
Low K
Moderate K
High K
G
TCGA (n = 110 patients)
MGC^High n = 11
MGC^Int n = 18
MGC^Low n = 81
Overall survival
Log-rank test for trend P value = 0,0224
Days from surgery
H
GR (n = 284 patients)
MGC^High n = 40
MGC^Int n = 65
MGC^Low n = 179
Overall survival
Log-rank test for trend P value = 0,0124
Days from surgery
I
TCGA + GR (n = 394 patients)
MGC^High n = 51
MGC^Int n = 83
MGC^Low n = 260
Overall survival
Log-rank test for trend P value = 0,0007
Days from surgery
J
TCGA + GR (n = 394 patients)
MGC^High n = 51
MGC^Int n = 83
MGC^Low n = 260
Progression-free interval
Log-rank test for trend P value < 0,0001
Days from surgery
0
50
100
0
500
1,000
1,500
2,000
K
Patients
Neoadjuvant therapy
Surgery
Adjuvant therapy
L
GR
Oral cavity cohort
Induction chemotherapy
(n = 52 patients)
No residual tumor
(n = 9)
Residual tumor
(n = 43)
MGC^High
(n = 21)
MGC^Low/Int
(n = 22)
M
Good response to ICT
Keratin
MGC
N
Groups proportion (%)
0.0
0.2
0.4
0.6
0.8
1.0
MGC^High
MGC^Low/Int
No residual tumor
TCGA + GR - naive
GR - induction CT
O
MGC^High n = 21
MGC^Low/Int n = 22
No residual tumor n = 9
Overall survival
Log-rank test MGC^High and MGC^Low/Int
P value = 0,0022
Days from surgery
P
Proportion of MGC groups (%)
MGC^High
MGC^Low/Int
Poor response (n = 17)
Good/partial response (n = 35)

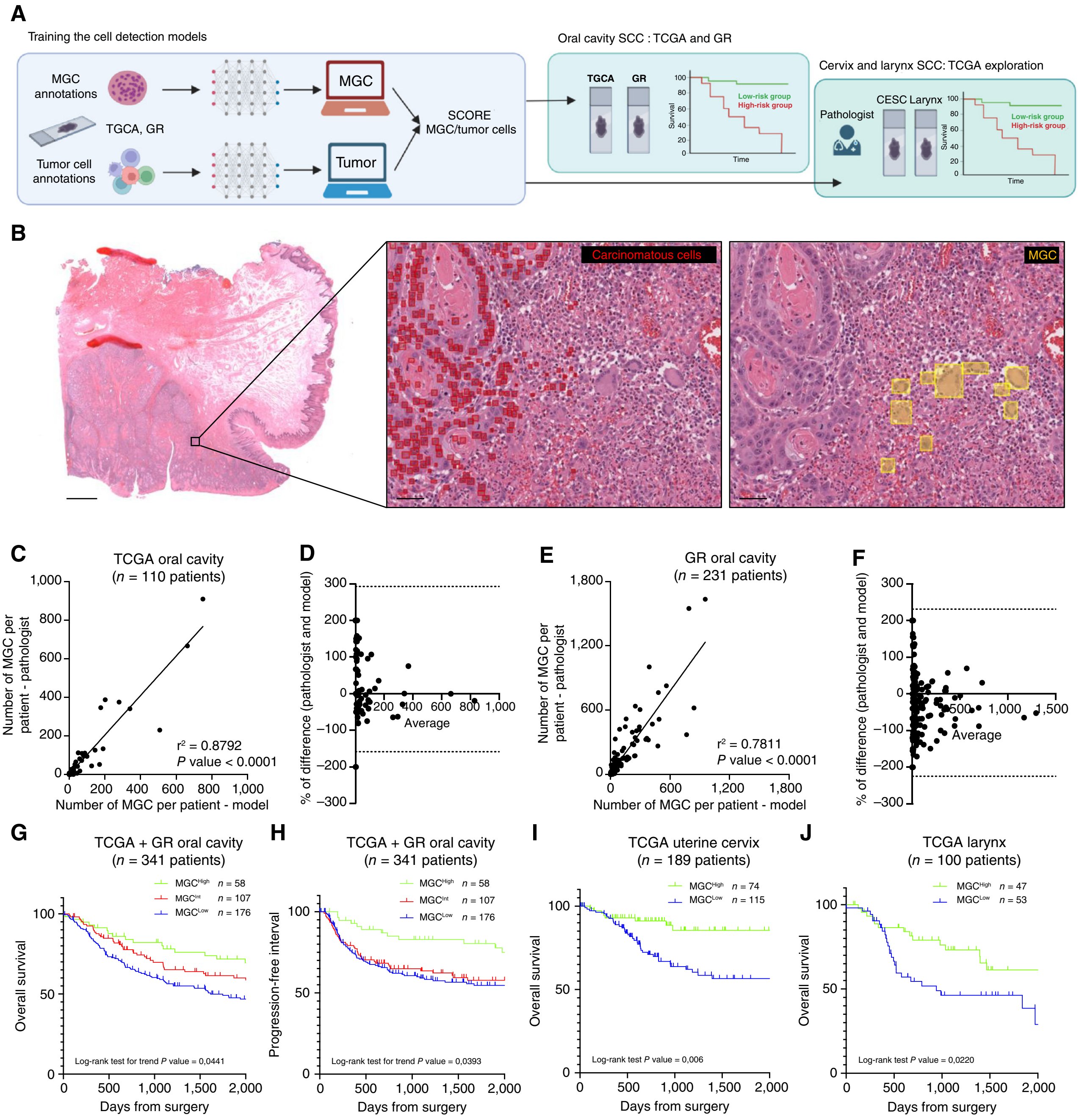

Figure 2. Automatic detection of MGC and tumor cells on H&E/HES whole slide images by deep learning. **A,** Overview of the methodology. Manual annotations of MGC and tumor cells were used to train two cell detection models to identify and count MGC and carcinomatous cells in SCC. An automatic score was computed as the ratio of MGC to tumor cells. The score was applied first to TCGA and GR oral cavity cohorts and second to TCGA Uterine cervix and Larynx cohorts. **B,** Keratinizing oral SCC with granulomas, from the TCGA cohort. Left, low magnification of the carcinoma (scale bar, 2 mm). Middle, high magnification of the carcinoma where automatically detected carcinomatous cells are highlighted in red (scale bar, 50 μm). Right, high magnification of the carcinoma where automatically detected MGC are highlighted in yellow (scale bar, 50 μm). **C,** Correlation between the number of MGC per patient quantified manually by a pathologist and automatically detected by the model. Patients were from the oral cavity TCGA cohort (*n* = 110 patients). **D,** Bland-Altman plots for TCGA oral cavity data shown in **C**. **E,** Correlation between the number of MGC per patient quantified manually by a pathologist and automatically detected by the model. Patients are from the oral cavity GR cohort (*n* = 231 patients). **F,** Bland–Altman plots for the GR oral cavity data shown in **E**. **G,** OS curve of oral cavity TCGA and GR patients (*n* = 341 patients) stratified according to MGC density computed by the cell detection model. The vertical tick mark on the curves means that a patient was censored at this time. **H,** PFI curve of oral cavity TCGA and GR patients (*n* = 341 patients) stratified according to MGC density computed by the cell detection model. **I,** OS curve of Uterine cervix SCC TCGA patients (*n* = 189 patients) stratified according to MGC density computed by the cell detection model. **J,** OS curve of Larynx TCGA patients (*n* = 100 patients) stratified according to MGC density computed by the cell detection model.

rank-biserial correlation of 0.929 in TCGA and 0.867 in GR. The area under the ROC curve (AUC) between the predicted patient AI scores and the manually computed MGC^{Low} versus MGC$^{Int/High}$ was 0.990 in TCGA and 0.965 in GR, and 0.963 in TCGA and 0.909 in GR for MGC^{High} versus MGC$^{Low/Int}$. Accordingly, patients were efficiently stratified into MGC^{High}, MGC^{Int} and MGC^{Low} groups and the automatic MGC biomarker was associated with longer OS and PFI (Fig. 2G and H).

We then asked whether our automatic detection model could be used in Uterine cervix (CESC) and Larynx SCC. Initially, MGC predictions gave false positive MGC detections in both cervical and laryngeal SCC TCGA cohorts; due to tissue-specific features of the larynx and cervix that were absent in the oral cavity and so not included in the training data. We overcame this issue by calibrating the MGC detection model to increase its sensitivity. Doing so, we excluded the risk of false negatives, while leading to abundant (true and false) positives that were then manually corrected by a pathologist: although slower than full automation, this method was approximately 10 times faster compared to a pathologist-only approach (Supplementary Fig. S4D and S4E) and reached similar levels of accuracy (Supplementary Fig. S4F–S4I). Using this approach, we categorized patients into high and low MGC/tumor ratios and found that increased proportions of MGC again correlated with longer OS in both CESC and Larynx SCC (Fig. 2I and J) and with longer PFI in CESC (Supplementary Fig. S4J and S4K).

Altogether, our automatic cell detection approach was rapid and efficient, allowing easy assessment of the MGC-to-tumor cell ratio that acted as a clear biomarker of prognosis in patients with oral cavity, Uterine cervix, and Larynx SCC.

Spatial Transcriptomics Identifies MGC as a Specific Population of Macrophages

Having identified the relationship between MGC density and prognosis, we next wanted to investigate their biological function within the TME. We exploited Visium spatial transcriptomic technology (10x Genomics) to analyze the single giant cell transcriptomes of MGC, on formalin-fixed, paraffin-embedded (FFPE) HNSCC tumor sections (Fig. 3A and B). Such technology assesses transcriptomes on spots, directly on histological slides. Importantly, because the diameter of a Visium spot is 55 µm, this technology has a pseudo-single cell resolution. Here, we took advantage of this limit, as one spot corresponds roughly to the size of an individual MGC, allowing the definition of their specific transcriptomic signature.

We analyzed slides from nine patients: six MGC^{High} tumors and three MGC^{Low} (Fig. 3C–H). Unsupervised clustering revealed seven distinct clusters of cells that matched manual morphology-based annotations (Supplementary Table S8). When projected onto a Uniform Manifold Approximation and Projection for Dimension (UMAP) space, MGC formed a clear distinct cluster (Fig. 3I). Of note, MGC were the only cell type with significantly different abundance between MGC^{High} and MGC^{Low} tumor samples (Fig. 3J). To narrow MGC signature, spots only covering MGC were manually selected (Supplementary Fig. S5A) and were shown to overlap with the unsupervised analysis (Supplementary Fig. S5B). Differentially expressed genes (DEG) between annotated MGC spots and all non-MGC spots included *CHIT1*, *FBP1*, *MMP9*, *SPP1*, *APOE*, *CHI3L1*, *CTSS*, *CTSB*, *CTSD*, *CTSZ*, *TYROBP*, *CD68*, *DC-STAMP*, *MARCO*, and *TREM2* confirming their macrophage nature (Fig. 3K; Supplementary Table S9). Gene Ontology (GO) analysis of this supervised signature showed upregulation of pathways involved in bone resorption, tissue remodeling and extracellular matrix disassembly, as well as macrophage activation, phagocytosis, antigen presentation, and ROS production (Supplementary Fig. S5C).

To validate this signature, we investigated the transcriptomic differences between MGC^{High} and MGC^{Low} tumors from TCGA patients with oral cavity SCC. We retrieved the bulk RNA sequencing data (bulk RNA-seq) for 108 patients (out of the initial 110 patients, two did not have RNA-seq data) for which we had quantified MGC density on WSI. DEG analysis showed a clear difference between the bulk signatures of MGC^{High} and MGC^{Low} tumors (Fig. 3L). GO analysis of TCGA RNA bulk signature also highlighted pathways common to the Visium-defined MGC signature, such as bone resorption, tissue remodeling, and macrophage differentiation (Supplementary Fig. S5D). GSEA analyses showed a significant enrichment of the spatial transcriptomic MGC signature in MGC^{High} TCGA patients (Fig. 3M; Supplementary Fig. S5E). Among genes that were more highly expressed in MGC^{High} tumors were macrophage-related genes (*SPP1*, *MARCO*, *DC-STAMP*, *OSCAR*) and MGC-specific genes (*CHIT1*, *FBP1*), which confirmed our spatial transcriptomic data (Supplementary Fig. S5F). Because the prognostic impact of CHIT1 (16) and TREM2 (8) was recently reported, we investigated their potential influence and showed that *CHIT1* and *TREM2* were associated with a longer OS in TCGA oral cavity SCC cohort (Supplementary Fig. S5G). Of note, RNA expression of *CK5*, *CHIT1*, and *CD68* were validated at the protein level by immunohistochemistry (Supplementary Fig. S6A–S6C).

Taken together, these results revealed the core macrophage signature of MGC and suggested a potential antitumoral function through the expression of genes and proteins associated with phagocytosis, antigen presentation, keratin resorption, and tissue remodeling.

MGC-Related Tumor Microenvironment Is Enriched in CD4 TCM T cells and TREM2-Expressing Mononuclear Macrophages

We then investigated the composition of the TME associated with MGC presence using the CosMx 64-plex human immuno-oncology protein panel (Nanostring) on four MGC^{High} and four MGC^{Low} patients. We identified nine general cell clusters (Supplementary Fig. S7A–S7D). MGC exhibited a specific macrophage signature (Supplementary Fig. S7D). MGC^{Low} patients showed similar clusters, except for MGC (Supplementary Fig. S7E–S7G). Within the immune population, we found 14 cell subsets in MGC^{High} patients (Fig. 4A–D) and 12 in MGC^{Low} patients (Supplementary Fig. S7H and S7I). Notably, TCM CD4 T cells increased in MGC^{High} patients, clustering together in close contact with B cells (Fig. 4D–G). No significant differences were seen in other cell subsets. However, we observed in MGC^{High} patients, a noticeable but nonsignificant trend toward increased infiltration of B cells and plasma cells that were clustering together (Fig. 4H and I).

Additionally, we observed a marked increased in a mononuclear macrophage subset sharing a signature and localization with MGC (Fig. 4D, G, and J; Supplementary Fig. S8), termed MGC-MNP (Fig. 4K). To characterize deeper MGC and MGC-MNP, we performed a second multiplex imaging panel containing CHIT1, CD163, CD68, and TREM2 antibodies, in nine patients (four MGC^{High} and five MGC^{Low}). MGC and surrounding MGC-MNP expressed CHIT1 and TREM2 proteins (Fig. 4L and M; Supplementary Fig. S9A–S9C; Supplementary videos S1 and S2). These TREM2-expressing MGC-MNP were clustering with MGC in keratin-rich niches (Fig. 4N), leading us to speculate that they might be MGC precursors.

DISCUSSION

Herein, we observed in two cohorts of patients with HNSCC from TCGA (n = 110 patients) and GR (n = 284 patients) that the density of MGC associates with a longer OS and PFI. As in treatment-naive patients (n = 394), the association was also observed in preoperative chemotherapy-treated (n = 52) patients. To improved patient stratification, we developed a deep-learning approach to automatically quantify the MGC-to-tumor-cell ratio on standard H&E/HES WSI, which proved as effective and faster than manual pathologist assessment. We then investigated the MGC-related TME using spatial transcriptomic and proteomic: we found an increase in CD4 TCM T cells and TREM2^{High} TAM that share a signature and localization with MGC in keratin-enriched tumor niches and correlate with MGC abundance.

MGC accumulation is well documented in response to foreign body (17). Indeed, following its introduction, macrophages and monocytes fused to form foreign-body giant cells (17). In HNSCC, the carcinoma synthesizes the keratin that is seen as a foreign body by the immune system (10). However, it is not the presence of keratin *per se*, but rather of keratin-associated MGC that is associated with longer survival. Understanding why only a fraction of patients with keratinizing SCC have high MGC densities could reveal the missing steps of the foreign body reaction toward keratin, providing insights into the drivers of this antitumor program and paving the way for new treatments.

The presence of MGC in SCC after preoperative therapy has been long known (18) and is part of the histological scoring for pathological response following antitumor therapy (19). However, only recently a study in esophageal SCC highlighted MGC as the only factor associated with prolonged OS in multivariate analysis after preoperative therapy (20). In addition, two other recent studies suggest a positive impact of MGC in treatment-naive patients with SCC of the esophagus or tongue (12, 13). Here, we confirmed these observations and defined the first evidence-based threshold for the relationship between MGC density and patient risk, demonstrating its potential for informing therapeutic decisions.

Although the clinical relevance of MGC is emerging, their biology remains poorly understood. We analyzed the whole transcriptomes of individual MGC in HNSCC, revealing their specific “single giant cell RNA signature,” that share strong similarities with TREM2^{High} mononuclear macrophages. TREM2^{High} TAM are known to be protumoral in several cancers (8), including colorectal (21), breast (21–23), and lung (24) adenocarcinomas and are more abundant in patients with nonresponding melanomas treated by immunotherapy (25). Their deletion enhances the efficacy of immunotherapy in a model of ovarian adenocarcinoma (26). Interestingly, neither adenocarcinomas nor melanomas produce keratin. In contrast, we report a good prognosis for TREM2^{High} MGC in HNSCC—a carcinoma producing extracellular keratin. We found that TREM2^{High} TAM and MGC clustered in keratin-containing tumor niches, suggesting that keratin creates specific intratumoral niches leading to the accumulation of TREM2^{High} TAM, which then fuse into antitumoral MGC. These opposite prognosis values of TREM2^{High} macrophages across cancers highlight the specificity of each tumor type and underline that the protumoral and antitumoral features of macrophage populations cannot be generalized. Notably, it urges caution for current clinical trials of anti-TREM2 therapies in keratinizing SCC as they could hamper patient prognoses.

CHIT1 expression was shown to be associated with good prognosis in bulk RNA-seq data from three HNSCC cohorts (16) and elevated in the blood of good responder patients with HNSCC after radiotherapy (27). In addition, a population of CHIT1- and TREM2-expressing macrophages associated with complete response to neoadjuvant immunotherapy in patients with esophageal SCC (28). Here we confirmed the favorable impact of CHIT1 and *TREM2* on OS and identified MGC as a major source of CHIT1 production via single giant cell analysis.

Figure 3. Spatial transcriptomics reveals a unique MGC signature. **A,** Low magnification of a representative HES section of a carcinoma selected for spatial transcriptomic analysis. Inset, high magnification of an MGC. **B,** Same HES section with the overlay of the spots analyzed by Visium technology. One spot is covering a single MGC. **C,** Low magnification of a representative HES of an MGC^{High} carcinoma from a patient in the GR cohort. **D,** Overlay of the seven cell populations analyzed by unsupervised clustering. **E,** Same HES section showing pathologist annotations of the tumor area (blue) and the MGC (yellow). **F,** Low magnification of a representative HES of an MGC^{Low} carcinoma from a patient in the GR cohort. **G,** Overlay of the seven cell populations analyzed by unsupervised clustering. **H,** Same HES section showing pathologist annotations of the tumor area (blue). **I,** Projection of the Visium spots onto a UMAP space; spots from nine different patients. **J,** Histograms showing the number of spots capturing the different cell types in MGC^{High} and MGC^{Low} carcinomas. **K,** Volcano plot showing MGC RNA signature extracted from the DEG analysis between supervised MGC spots and all the other non-MGC spots. **L,** Volcano plot showing the DEG between MGC^{High} and MGC^{Low} tumors from patients in TCGA cohort (n = 108 patients). **M,** GSEA plot showing the enrichment of the Visium MGC signature in MGC^{High} vs. MGC^{Low} patients classified from TCGA. The green line represents the running enrichment score for the MGC signature, with the peak indicating maximum enrichment. The normalized enrichment score (NES) is 3.24, and the P value is 0.000522, demonstrating significant enrichment of the MGC signature in MGC^{High} patients. The barcode plot shows the positions of the MGC signature genes within the ranked list of genes from the bulk RNA sequencing data, with a higher density of genes towards the left, indicating higher enrichment.

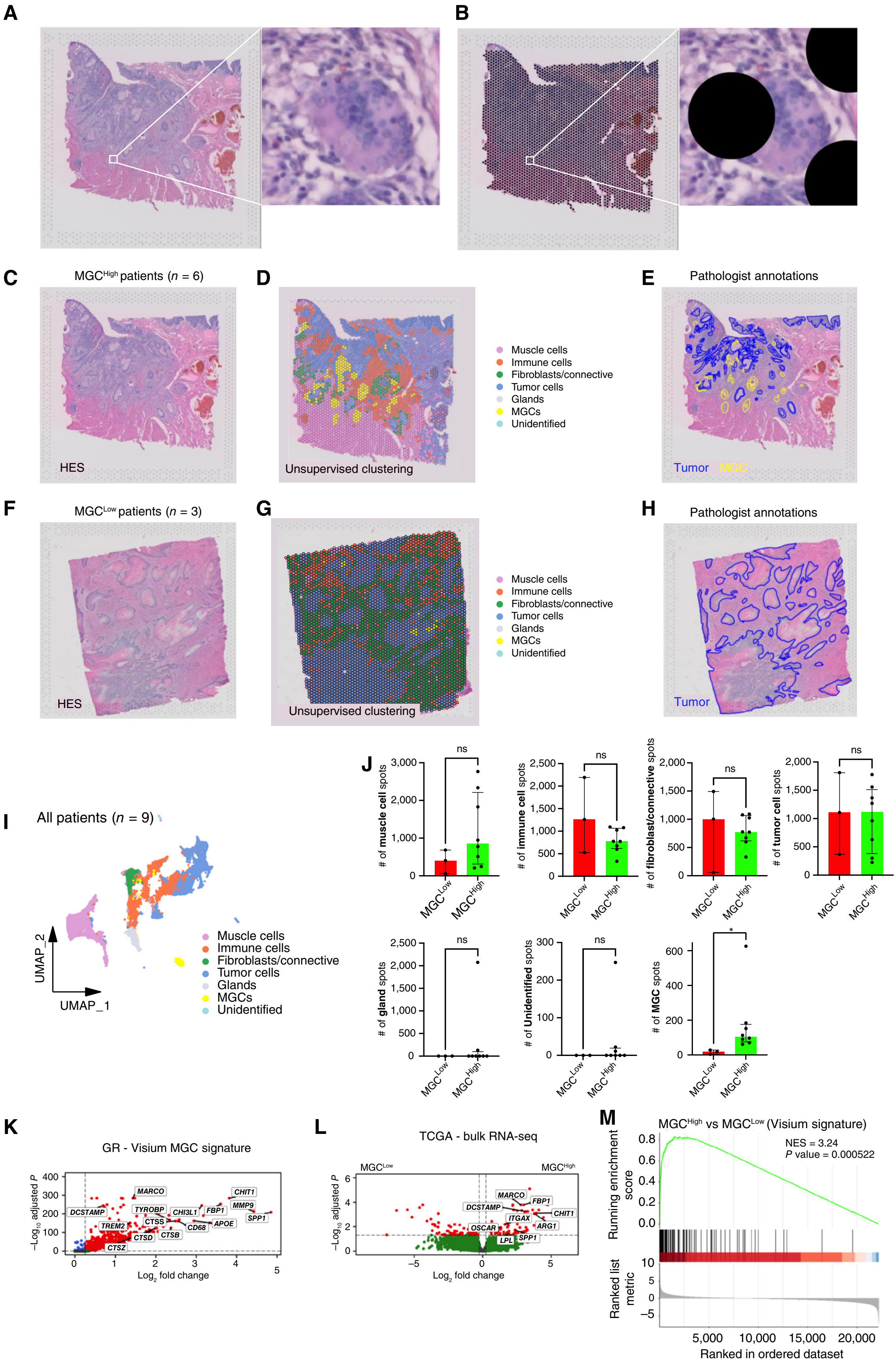
A
B
C
MGC^High patients (n = 6)
HES
D
Unsupervised clustering
Muscle cells
Immune cells
Fibroblasts/connective
Tumor cells
Glands
MGCs
Unidentified
E
Pathologist annotations
Tumor
MGC
F
MGC^Low patients (n = 3)
HES
G
Unsupervised clustering
H
Pathologist annotations
Tumor
I
All patients (n = 9)
UMAP_2
UMAP_1
J
# of muscle cell spots
# of immune cell spots
# of fibroblasts/connective spots
# of tumor cell spots
# of gland spots
# of Unidentified spots
# of MGC spots
ns
*
MGC^Low
MGC^High
K
GR - Visium MGC signature
−Log10 adjusted P
Log2 fold change
MARCO
CHIT1
DCSTAMP
TYROBP
CHI3L1
FBP1
MMP9
SPP1
TREM2
CTSS
CD68
APOE
CTSD
CTSB
CTSZ
L
TCGA - bulk RNA-seq
MGC^Low
MGC^High
MARCO
FBP1
DCSTAMP
CHIT1
ITGAX
ARG1
OSCAR
SPP1
LPL
M
MGC^High vs MGC^Low (Visium signature)
NES = 3.24
P value = 0.000522
Running enrichment score
Ranked list metric
Ranked in ordered dataset

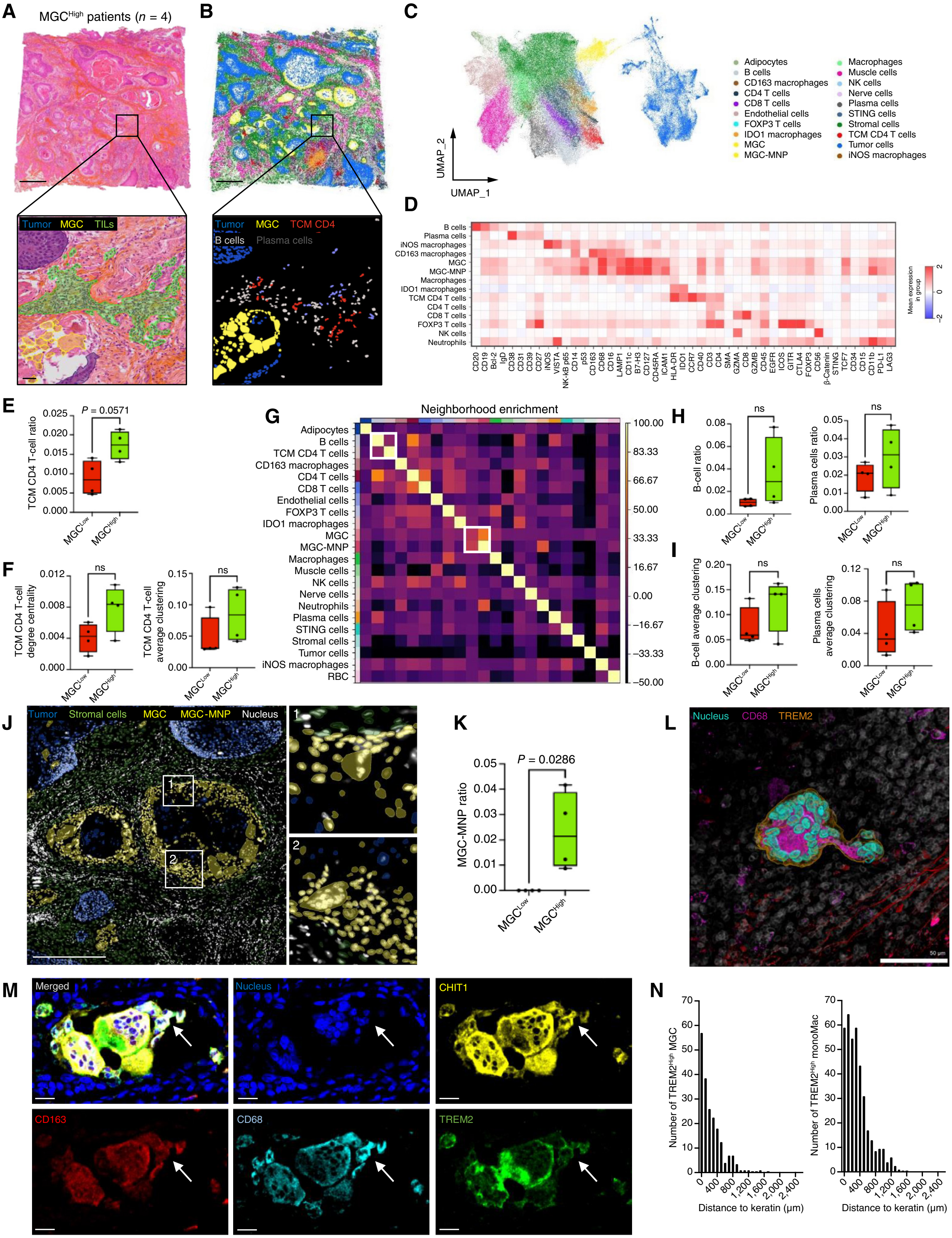
A
MGC^High patients (n = 4)
Tumor MGC TILs
B
Tumor MGC TCM CD4
B cells Plasma cells
C
UMAP_2
UMAP_1
Adipocytes
B cells
CD163 macrophages
CD4 T cells
CD8 T cells
Endothelial cells
FOXP3 T cells
IDO1 macrophages
MGC
MGC-MNP
Macrophages
Muscle cells
NK cells
Nerve cells
Plasma cells
STING cells
Stromal cells
TCM CD4 T cells
Tumor cells
iNOS macrophages
D
B cells
Plasma cells
iNOS macrophages
CD163 macrophages
MGC
MGC-MNP
Macrophages
IDO1 macrophages
TCM CD4 T cells
CD4 T cells
CD8 T cells
FOXP3 T cells
NK cells
Neutrophils
CD20 CD19 Bcl-2 IgD CD38 CD31 CD39 CD27 iNOS VISTA NK-kB p65 CD14 p53 CD163 CD68 CD16 LAMP1 CD11c B7-H3 CD127 CD45RA ICAM1 HLA-DR IDO1 CCR7 CD40 CD3 CD4 SMA GZMA CD8 GZMB CD45 EGFR ICOS GITR CTLA4 FOXP3 CD56 β-Catenin STING TCF7 CD34 CD15 CD11b PD-L1 LAG3
Mean expression in group
2 0 −2
E
TCM CD4 T-cell ratio
P = 0.0571
0.025 0.020 0.015 0.010 0.005 0.000
MGC^Low MGC^High
F
TCM CD4 T-cell degree centrality
ns
0.012 0.008 0.004 0.000
TCM CD4 T-cell average clustering
ns
0.15 0.10 0.05 0.00
MGC^Low MGC^High
G
Neighborhood enrichment
Adipocytes
B cells
TCM CD4 T cells
CD163 macrophages
CD4 T cells
CD8 T cells
Endothelial cells
FOXP3 T cells
IDO1 macrophages
MGC
MGC-MNP
Macrophages
Muscle cells
NK cells
Nerve cells
Neutrophils
Plasma cells
STING cells
Stromal cells
Tumor cells
iNOS macrophages
RBC
100.00 83.33 66.67 50.00 33.33 16.67 0.00 −16.67 −33.33 −50.00
H
B-cell ratio
ns
0.08 0.06 0.04 0.02 0.00
Plasma cells ratio
ns
0.05 0.04 0.03 0.02 0.01 0.00
MGC^Low MGC^High
I
B-cell average clustering
ns
0.20 0.15 0.10 0.05 0.00
Plasma cells average clustering
ns
0.12 0.08 0.04 0.00
MGC^Low MGC^High
J
Tumor Stromal cells MGC MGC-MNP Nucleus
1
2
K
MGC-MNP ratio
P = 0.0286
0.05 0.04 0.03 0.02 0.01 0.00
MGC^Low MGC^High
L
Nucleus CD68 TREM2
50 μm
M
Merged
Nucleus
CHIT1
CD163
CD68
TREM2
N
Number of TREM2^High MGC
70 60 50 40 30 20 10 0
Distance to keratin (μm)
0 400 800 1,200 1,600 2,000 2,400
Number of TREM2^High monoMac
70 60 50 40 30 20 10 0
Distance to keratin (μm)
0 400 800 1,200 1,600 2,000 2,400

In line with previous results (29, 30), we showed that MGC$^{\text{High}}$ patients had high levels of TILs. We then explored the contribution of each lymphoid cell subset using high-throughput multiplex analysis. We highlighted an increase in TCM CD4 T cells in MGC$^{\text{High}}$ patients, which were found in proximity to B-cell clusters. Notably, a recent study highlighted the expansion of TCM CD4 T cells, B cells, and plasma cells in patients with HNSCC treated with a combination of anti-CTLA4 and anti-PD-L1 (31). Furthermore, tumor-infiltrating TCM CD4 T cells have been associated with favorable prognosis in OSCC (32). Collectively, the increase of these immune cell ecosystems, composed of TCM CD4 T cells, B cells, and plasma cells, may contribute to the favorable prognosis in patients with high MGC density.

The digitization of pathology laboratories opens the way for AI algorithms to improve diagnostic and prognostic (33). Manual quantification of MGC is time-consuming for overwhelmed pathologists (34) and impossible to apply in routine. Thus, we designed a deep learning model to quantify the MGC-to-tumor cell ratio automatically on routine diagnostic WSI stained by H&E/HES, without the need for additional costly techniques such as immunohistochemistry or genetic testing. This approach is faster, yet equally efficient as pathologists, and effectively stratifies patients. Pending further validations in additional HNSCC cohorts from different centers, this method could identify patients in need of therapeutic optimization based on predicted risk level.

Lastly, because SCC is widely spread across the body, we took advantage of our deep learning model to screen for the presence of MGC in laryngeal SCC and CESC. Consistent with previous esophageal publications (11, 20), MGC density indicated favorable prognosis in SCC of Larynx and Uterine cervix. Robust validation on external cohorts is required.

To conclude, TREM2$^{\text{High}}$ MGC are major contributors to good prognosis in treatment-naive and preoperatively treated SCC, and their monitoring will be of tremendous value to improve the clinical management of patients suffering from HNSCC.

METHODS

Patients

TCGA Oral Cavity Cohorts. Data from 527 patients with HNSCC were retrieved from the TCGA website. Exclusion criteria were patients with only frozen sections, low quality slides, no diagnostic slides, absence of surgical resection, only biopsies, HPV-positive tumors, or tumor localization elsewhere than oral cavity: this led to exclusion of 417 patients, leaving data from 110 patients eligible for further analyses (Supplementary Table S1). These patients were considered "treatment-naïve" because they did not receive preoperative therapy. All slides were stained by H&E. We had access to the bulk RNA-seq data for 108 of these patients. These patients had a median follow-up of 34 months (interquartile range 21; 56 months).

TCGA Larynx and CESC Cohorts. Data from 307 patients with uterine cervix carcinoma and from 527 patients with HNSCC were retrieved from TCGA. Exclusion criteria for uterine cervix were patients without squamous cell carcinoma, frozen sections, low quality slides, and no diagnostic slides: this led to the exclusion of 118 patients, leaving data from 189 patients eligible for further analyses. Exclusion criteria for Larynx were frozen sections, low quality slides, no diagnostic slides, and tumor localization elsewhere than larynx: this led to exclusion of 427 patients, leaving data from 100 patients eligible for further analyses. All slides were stained by H&E.

GR Cohorts. We had access to samples from two previously published cohorts of patients with HNSCC treated at GR (14, 15). These patients did not receive preoperative therapy and were thus considered as "treatment-naive." Exclusion criteria were patients with not enough representative pathological diagnostic slides, low quality slides, or the presence of neoadjuvant therapy: out of 419 patients, 284 were included (Supplementary Table S1). These patients had a median follow-up of 113 months (interquartile range 81; 150 months). We further had access to a retrospective cohort of 52 patients with HNSCC treated by ICT at GR. All FFPE blocks and slides came from the pathology laboratory of GR and were stained by HES. All patients gave a written informed consent. For each patient, the study protocol was approved by the institutional review board of GR (IRB-2023-293). All experiments were in accordance with the Declaration of Helsinki. The REporting recommendations for tumor MARKer prognostic studies were followed.

Pathologist Annotations and Quantifications

MGC and Tumor Surface Quantification. A pathologist quantified the MGC per mm^2 of tumor for each H&E/HES slide from each patient from TCGA ($n = 110$ slides) and GR cohorts ($n = 1{,}304$ slides). A second pathologist quantified the MGC per mm^2 of tumor for a subset of the patients (TCGA $n = 10$ slides; GR $n = 20$ slides): the counts from the two pathologists showed almost perfect agreement ($r^2 = 0.9606$, P value<0.0001 and weighted kappa = 0.876; Supplementary Fig. S10A and S10B).

MGC-related stratification was based on two thresholds for manual quantification: MGC$^{\text{High}}$ (≥1 MGC/mm^2), MGC$^{\text{Int}}$ (≥0.2 MGC/mm^2 and <1 MGC/mm^2), and MGC$^{\text{Low}}$ (<0.2 MGC/mm^2). The threshold

Figure 4. MGC-related tumor microenvironment is enriched in CD4 TCM T cells and TREM2-expressing mononuclear macrophages. **A,** Low magnification of a representative HES section MGC$^{\text{High}}$ carcinoma selected for CosMx 64-plex protein panel analysis. Scale bar, 500 μm. Inset, high magnification of an area annotated by a pathologist, enriched in TILs (green) close to tumor cells (blue) and a granuloma with MGC (yellow). Scale bar, 50 μm. **B,** Low magnification of the same tumor section, stained by the CosMx protein panel, with the overlay of 20 cell populations (non-immune and immune). Scale bar, 500 μm. Inset, high magnification of the same area, with the annotation overlay of tumor cells, MGC (yellow), TCM CD4 T cells (red), B cells (light gray) and plasma cells (dark gray). **C,** Projection of the CosMx cell population onto a UMAP space. **D,** Heat maps showing the expression of immune markers across the 14 immune cell types. Red indicates a higher expression and blue a bottom expression. **E,** Box-plot showing the TCM CD4 T cells ratio between MGC$^{\text{Low}}$ ($n = 4$) and MGC$^{\text{High}}$ patients ($n = 4$). **F,** Box-plot showing TCM CD4 T cells degree centrality (left) and average clustering (right) between MGC$^{\text{Low}}$ ($n = 4$) and MGC$^{\text{High}}$ patients ($n = 4$). **G,** Heat maps of neighborhood enrichment scores showing the spatial colocalization of the 22 cell types across four MGC$^{\text{High}}$ patients. Yellow indicates a high enrichment and purple a low enrichment. White boxes are highlighting the proximity between (i) TCM CD4 T cells and B cells and (ii) MGC and MGC-MNP. **H,** Box plots showing B cells (left) and plasma cells ratio (right) between MGC$^{\text{Low}}$ ($n = 4$) and MGC$^{\text{High}}$ patients ($n = 4$). **I,** Box plots showing B cells (left) and plasma cells average clustering between MGC$^{\text{Low}}$ ($n = 4$) and MGC$^{\text{High}}$ patients ($n = 4$). **J,** Low magnification of a representative section stained by the CosMx protein panel, of two granulomas, with the annotation overlay of tumor cells (blue), stromal cells (green), MGC and MGC-MNP (yellow). Insets: high magnification showing MGC surrounded by numerous MGC-MNP. Scale bar, 800 μm. **K,** Box-plot showing the MGC-MNP ratio between MGC$^{\text{Low}}$ ($n = 4$) and MGC$^{\text{High}}$ patients ($n = 4$). **L,** Representative image of a single MGC stained by CD68 (pink), TREM2 (orange), and Hoechst (cyan). The merge image is shown (scale bar, 50 μm). **M,** Representative high magnification image of a small granuloma. The arrow indicates mononuclear macrophages (scale bar, 20 μm). **N,** Histograms showing the distance of TREM2$^{\text{High}}$ MGC from keratin (left) and histograms showing the distance of TREM2$^{\text{High}}$ mononuclear macrophages from keratin (right).

of 0.2 was selected using the maximally selected rank statistics, on the OS endpoint in the combined TCGA and GR cohorts (n = 394 patients). The threshold of 1 was selected to obtain a group of more than 50 patients with very high MGC densities.

The annotations were carried out with QuPath version 0.4.3, an open-source software for digital pathology images analysis (35).

Stratification of patients treated by ICT into good, partial, and poor responders was made by a pathologist using the original grading system published by Braun and colleagues (19).

TILs Quantification. Two pathologists quantified the TILs on H&E/HES slide for each TCGA (n = 110 slides) and GR patients (n = 1,304 slides). TILs were evaluated according to a scoring method developed by the International Immuno-Oncology Biomarkers Working group (36). TILs were scored as the percentage of surface occupied by lymphocytes. Only the tumor and tumor-related stroma were included in the analysis. The percentage of TILs was assessed semiquantitatively from 0% to 100%. Challenging cases were reviewed by the two pathologists until an agreement was reached.

Tumor Grade Quantification. Two pathologists quantified the tumor grade on H&E/HES slides for each TCGA (n = 110 slides) and GR patients (n = 1,304 slides). Grade was evaluated according to the fifth edition of the WHO that is based on the similarity to healthy squamous epithelium as described by Broder in 1920 (37). Squamous cell carcinoma was graded in well (G1: grade 1), moderate (G2: grade 2), and poorly (G3: grade 3) differentiated tumors. Challenging cases were reviewed by the two pathologists until an agreement was reached.

Digitization of HES Pathological Slides

We retrieved the 1,304 physical microscopic slides from the two cohorts of treatment-naïve patients from GR (14, 15). Multiple slides per patient were available (range 1–17). While most of the slides had a standard microscopic size (75 × 25 mm), several of them were larger (75 × 50 mm) and did not physically fit into the digital slide scanner. Therefore, all large microscope slides were removed from the analysis and 44 patients with large slides only were excluded from the digital analysis. Quality control was performed by a pathologist to exclude slides with common artifacts such as tissue folds, blurring or faint staining, resulting in the exclusion of nine additional patients. Overall, 839 slides were analyzed, representing tumors from 231 patients (of the original 284 included patients). Slides were digitized at 20× resolution, with an Olympus VS120.

Slides from TCGA cohort were already digitized and one slide per patient was quantified (n = 110 patients and n = 110 slides).

Training of Deep Learning Models

Training Data for MGC. To train the MGC detection model, 16 oral cavity WSI from TCGA and 12 oral cavity WSI from the GR cohort were retrieved. A pathologist annotated a total of 5,000 MGC by drawing bounding boxes using QuPath software version 0.4.3. Rather than exhaustively annotating all MGC in a small number of slides, we opted to maximize the variability by nonexhaustively annotating some of the MGC on many slides. The annotation instructions were to draw bounding boxes around each MGC and then to draw an englobing bounding box that ensured that all MGC were exhaustively annotated in the latter. As such, all pixels outside the englobing boxes were not used to train the detection model. We randomly annotated additional negative patches, i.e., patches that contained no MGC, by drawing an englobing bounding box. All englobing bounding boxes were extracted with both tissue image and annotations using an in-house software at 20×, resulting in fields of view (FOV) with varying size and with exhaustively annotated MGC. All FOV of 20 WSI were randomly assigned to the training set and the remainder FOV from eight WSI to the validation set. All the training and validation slides from the GR cohort that were used to train the MGC detection model were discarded from the rest of the study.

Training Data for Tumor Cells. The same protocol was applied to obtain ground-truth annotations for training the tumor detection model. In total, 814,606 tumor cells were collected from 15 WSI of TCGA tongue and 52 WSI of the GR cohort. Additionally, a pathologist exhaustively annotated the viable tumor cells in 107 WSI from the GR cohort, ensuring that there were not any tumor cells outside the annotated regions. Patches outside the annotated regions were added to the training data with an associated empty ground-truth since these patches do not contain tumor cells. The final training data contained 13,624 256 × 256 pixels patches with at least one tumor cell and 106,000 patches without tumor cells. All FOV of 47 WSI were randomly assigned to the training set and FOV from the remainder 20 WSI to the validation set. Here again, all the training and validation GR slides for the tumor detection model were discarded from the rest of the study.

Model Architecture and Hyper Parameters. We trained the Fully Convolutional One-Stage (FCOS; ref. 38) detection architecture for both tumor cells and MGC automatic annotation. Contrary to region proposal models, detections of FCOS are made at the pixel level: each pixel notably produces four values that are reconstructed as a predicted bounding box and an additional probability value for each class—1 in our case for both tumor and MGC. During training, each proposed bounding box is first matched with one ground-truth bounding box or no bounding box. Then, a regression loss and a classification loss are computed based on the predicted box coordinates and its associated probability. We used the ResNet50 architecture (39) pretrained on ImageNet (40) as the backbone model. Both classification and regression heads comprised four ReLU-activated convolutional layers of kernel size 3 and stride 1, with batch normalization. Contrary to the original implementation of FCOS, image rescaling was discarded to input patches with the same magnification as the model. Data augmentation consisted of rotations, flips, shifts, and color jitter. For each input patch, the same data augmentation was performed to the associated ground-truth bounding boxes using the Albumentations (41) Python library version 1.2.1. The detection model parameters were stochastically updated using the Adam optimizer (42) from errors computed by the focal loss (43) cost function with a learning rate of 10^{-4}, a regularization of 10^{-4} and a batch size of four patches. Training was conducted for up to 2,000 epochs on a NVIDIA A40 GPU. We selected the model snapshot with the maximum mean average precision at intersection-over-union of 0.5 (mAP@50) on the validation set for both tumor and MGC tasks for the remainder of our study. All deep learning implementation was done in Python 3.8, PyTorch (44) version 1.13, and Torchvision version 0.14.0.

Cell Detection Model Performances. We assessed the performances of the MGC and tumor cell detection model. Briefly, ground truth MGC and tumor cells (annotated by a pathologist) were compared to automatically detected MGC and tumor cells and the average precision was computed using the MMdetection package version 3.1.0 (arXiv 1906.07155). To assess further the performance of the MGC detection model, we compared the number of automatically detected MGC to the number of MGC that were quantified by a pathologist (Fig. 2C–F).

AI-Based Biomarker Inference

Once both tumor detection and MGC detection models were trained, the biomarker was computed for each WSI as follows. Patches of width 2,048 pixels were extracted from a WSI in a sliding window fashion with an overlap of 256 pixels for both sides. We used a non-zero overlap to remove border artifacts (such as false positives) arising from a lack of context at the borders. Each patch was forwarded into both the tumor and MGC models, producing two lists of predicting bounding box coordinates and their predicted probabilities. Bounding boxes predicted with a probability below 0.4 were discarded and we applied non-maximum suppression with a threshold of 0.6 intersection-over-union to remove highly overlapping predictions. We finally computed the proposed MGC biomarker as the ratio of the number of predicted MGC to the number of predicted tumor cells for each patient.

Spatial Transcriptomics

Library Preparation. The Visium Spatial Gene Expression Slide, Visium FFPE Reagent Kit, and Visium Human Transcriptome Probe Kit (10x Genomics) were used to generate sequencing libraries. RNA quality was accessed for all samples using the DV200 method. For library construction, 5 µm cryosections of 6.5 × 6.5 mm from each FFPE sample were placed into the four capture areas of the Spatial Transcriptomics slides (10x Genomics). Samples were then deparaffinized, stained, imaged, and decrosslinked. Probe hybridization and ligation to RNA were then performed, followed by the single-stranded ligation product release and extension. Libraries were then prepared following the manufacturer's instructions. All the libraries were sequenced with a 10-base index read (dual index), a 28-base Read1 containing cell-identifying barcodes and unique molecular identifiers (UMI), and a 90-base Read2 containing transcript sequences on an Illumina NovaSeq 6000.

Visium Data Analysis. All sections were processed individually using the Seurat package, with spots containing less than 500 UMI and 500 RNA counts were discarded from further analyses. Afterward, all slides were merged into one object used for DEG analysis and integration was based on the slide ID. For this, reciprocal principal component analysis (PCA) integration based on 30 first PCA dimensions, with k.anchor = 20 was performed. The Loupe software (10x Genomics) was used to explore the data.

Identification of MGC Signature. To identify the DEG between MGC spots and non-MGC spots, we used the R package Seurat, and the volcano plot was plotted using the Enhanced Volcano R package. Only the genes with a log2 fold change ($\log_2$FC) over 0.25 and an adjusted *P* value less than 0.05 were considered significant.

TCGA Bulk RNA-seq Data

Preprocessing of Data. Bulk RNA-seq data of primary tumors from 108 out of the 110 patients with tongue SCC were used for survival analysis. Data were retrieved using TCGABiolinks R package, then normalized using the EDAseq package based on gene length; genes whose expression was zero in more than 25% of the samples were removed.

Differentially Expressed Genes. The 108 patients with available histological slides were split into three groups based on the presence of MGC as annotated by a pathologist. DEGs were calculated between groups using the R package DESeq2, and the volcano plot was plotted using the Enhanced Volcano R package. Only genes with a $\log_2$FC higher than 0.25 and an adjusted *P* value less than 0.05 were considered significant.

Gene Set Enrichment Analysis. The patients were separated based on the pathology score of MGC$^{\text{High}}$ and MGC$^{\text{Low}}$. Differential expression analysis was performed with DESeq2, Logarithm fold changes were modified by the lfcShrink algorithm with the "Ashr" option. DEG cutoff was defined at an FDR less than 0.05 and an absolute $\log_2$FC value greater than 1 in pairwise comparisons. R package clusterprofiler (4.12) was used to analyze the DEGs between different groups for GO analyses. For the Visium GO analysis, only genes with $\log_2$FC superior to 1.5 were considered.

Venn Diagram Analysis. The analysis was made in the interactivenn website (45). The top DEG whose adjusted *P* value was lower than 0.05 and $\log_2$FC higher than 0.25 were extracted from TCGA bulk RNA-seq data and from the Visium MGC signature.

Multiplex Immunofluorescence

5-Plex Protein Panel Performed in GR. Nine FFPE blocks of HNSCC (four MGC$^{\text{High}}$ patients and five MGC$^{\text{Low}}$ patients) were stained by multiplex immunofluorescence. The Experimental and Translational Pathology Platform of GR performed the stainings using a preset routine protocol. Briefly, FFPE blocks were cut into 3-µm-thick sections. Multiplex staining was performed on a Bond RX (Leica Biosystems). Slides were baked in high pH for 20 minutes at 100°C for epitope retrieval. Then, multiple rounds of staining were performed. Each round included endogenous peroxidase blocking for 10 minutes, nonspecific sites blocking for 5 minutes, primary antibody incubation, secondary HRP-labeled antibody incubation for 10 minutes and OPAL reactive fluorophore incubation for 10 minutes to covalently label the primary epitope, and heat denaturation of antibodies. The sequence of the antibodies with the associated Opal dyes is as follow: (i) rabbit anti-TREM2 (clone D814C; Cell Signaling, reference 91068), 1/400 dilution, 1 hours, 37°C, with OPAL 520, 1/100 dilution; (ii) rabbit anti-CHIT1 (polyclonal; Biorbyt, reference orb377995), 1/50 dilution, 30 minutes, ambient temperature, with OPAL 570, 1/100 dilution; (iii) mouse anti-CD68 (clone KP1; DAKO, reference M0814), 1/1,000 dilution, 1 hours, ambient temperature, with OPAL480; (iv) mouse anti-CD163 (clone 10D6; Diagnostic BioSystems, reference Mob 460-05), 1/600 dilution, 15 minutes ambient temperature, with OPAL690, 1/100 dilution. Nuclei were visualized by a final incubation with the Spectral DAPI (Akoya Biosciences) for 5 minutes. Slides were mounted with mounting medium for fluorescence. Finally, images were acquired on the Polaris 2 (Akoya Biosciences).

64-Plex Protein Panel Performed in GR. Eight FFPE blocks of HNSCC (four MGC$^{\text{High}}$ patients and four MGC$^{\text{Low}}$ patients) were stained by multiplex immunofluorescence. The stainings were performed with the CosMx SMI 64-plex Human Immuno-Oncology Protein Panel. For each patient, two serial slides were cut: one slide stained by immunofluorescence and one slide stained by HES.

Immunofluorescence Performed in Erlangen. HNSCC tissue samples were cut into 500-µm-thick sections using a custom-made tissue slicer. Samples were permeabilized and blocked using 0.3% Triton-X-100 (Sigma) in PBS (Gibco) including 5% rat serum (Sigma) overnight at room temperature. Same buffer was used for immunostaining with anti-TREM2 followed by AlexaFluor-conjugated Fab Fragment Goat Anti-Rabbit IgG (Jackson ImmunoResearch), anti-CD68 (clone Y1/82A; BioLegend), and Hoechst (Biolegend) for 3 days at room temperature. After rigorous washing, samples were cleared for 3 hours using Ce3D (BioLegend). Imaging was performed using a Zeiss LSM 880 confocal microscope with a Plan-Apochromat 20×/1,0 objective at Nyquist rate. Individual channels were deconvolved using Huygens 22.10 (Scientific Volume Imaging) at default settings. Visualizations were done using ZEISS arivis Pro/Vision4d (Zeiss).

Multiplex Immunofluorescence Image Analysis

5-Plex Protein Panel. A pathologist manually annotated the tumor, the keratin, and the technical artifact regions on the nine immunofluorescence images, using QuPath v0.4.3 (35). In addition, a small proportion of TREM2-expressing mononuclear macrophages and MGC were manually annotated by a pathologist. These annotations were used to train a pixel classifier based on a random forest model. The classifier model was applied to predict the presence of TREM2-expressing MGC and mononuclear macrophages, in the tumor regions of the nine immunofluorescence images. Measurements of the areas and distances of these regions to the closest keratin-rich regions were exported and analyzed with a homemade R script (https://www.r-project.org) to produce graphics of surface ratios and distances to keratin regions.

64-Plex Protein Panel. A pathologist manually annotated the MGC and the tumor regions. Cell annotation was based on the combination of protein expression and cell localization on the HES slide. Images were processed and analyzed using the SOPA pipeline (46). Annotation of the cells was performed in two layers, focusing on the immune fraction of the slide. For the neighborhood analysis, we used the squidpy analysis (47).

Immunohistochemistry

CD68 Immunohistochemistry. Among the 284 patients from GR, 264 of them had available FFPE blocks. One representative slide per patient was selected by a pathologist. Patients without available FFPE blocks were excluded from the analysis (n = 20). Slides were stained with anti-CD68 antibody (clone KP1, DAKO, reference M0814), 1/1,000 dilution, 1 hours, 36°C.

CHIT1, CD68, and CK5 Immunohistochemistry. For each patient analyzed by Visium, three serial slides were stained with anti-CHIT1 antibody (polyclonal; Biorbyt, reference orb377995), 1/50 dilution, 30 minutes, 36°C; anti-CD68 antibody (clone KP1; DAKO, reference M0814), 1/1,000 dilution, 1 hour, 36°C;and anti-CK5 antibody (clone SP27; Roche, reference 760-4935), prediluted antibody (0,17 µg/mL), 32 minutes, 36°C.

Immunohistochemistry Protocol. The Experimental and Translational Pathology Platform of GR performed the stainings using a preset routine protocol. Briefly, FFPE blocks were cut into 3-µm-thick sections. Staining was performed on an ULTRA BenchMark (Roche Diagnostics). After deparaffinization, slides were baked in CC1 solution (pH 8, 20 minutes, 95°C) for epitope retrieval. Endogenous peroxidase activity was inhibited with peroxidase blocking reagent (UltraView DAB kit). Slides were then incubated with a primary antibody followed by a secondary antibody. 3,3′-Diaminobenzidine tetrahydrochloride was used for revelation and hematoxylin was used for counterstaining (UltraView DAB kit). Finally, slides were mounted with mounting medium (Pertex) and glass coverslips.

Immunohistochemistry Analysis

A pathologist annotated the tumor region in each slide, and the nontumoral regions were excluded from the analysis. The intensity of the CD68 staining per tumor surface was quantified. The intensity of CD68 in MGC was removed from the analysis. The analysis was performed with QuPath v0.4.3.

Survival Analyses

OS and PFI were the two clinical endpoints used for the analysis. Log-rank test and log-rank test for trend were performed. Multivariable survival analyses were also performed using Cox model and P value of Wald test was presented. Linear relationship between the log-hazard and MGC density and square root of MGC density were tested with a smoothing spline, using the pspline function of coxph in R survival package. For survival curves graphical representation, data were truncated at 2,000 days; however, tests were performed with all the length of the follow-up.

TCGA Cohorts. Clinical data were retrieved from the GDC Data Portal (https://portal.gdc.cancer.gov/). OS and PFI were retrieved from an integrated TCGA pan-cancer clinical data resource (48) in which the authors recommended using OS and PFI as clinical endpoints. PFI was defined as follows: “1 for patient having a new tumor event whether it was a progression of disease, local recurrence, distant metastasis, new primary tumors all sites, or died with the cancer without new tumor event, including cases with a new tumor event whose type is N/A. 0 for censored otherwise” (48).

GR Cohorts. Clinical data of treatment-naive patients were retrieved from the two ancillary annotated cohorts (14, 15). PFI was defined as follows: “events for progression or 2nd HNSCC or death by HNSCC or death of unknown cause with HNSCC”. GR clinical data of ICT patients were retrieved from the GR patient’s database.

Data Availability

Digital Slides. WSI were generated from publicly available cohorts (TCGA) and from institutional cohorts (GR). The digital WSI from TCGA are publicly accessible through the NIH Genomic Data Commons Data Portal https://portal.gdc.cancer.gov/. The digital WSI generated from GR cohorts are not publicly available due to general data protection regulations and institutional guidelines. Availability could be made upon request to the lead contact after execution of a data transfer agreement with GR.

Bulk RNA-seq Data. Data from TCGA can be retrieved from their website.

Visium RNA-seq Data. All generated Visium RNA-seq data are available and have been deposited in the functional genomics data collection (Array Express) under accession number E-MTAB-14409 (https://www.ebi.ac.uk/biostudies/arrayexpress/studies/E-MTAB-14409?key=dcc24ea4-8654-4f29-a4b1-26cdb071a1a5).

CosMx Protein Data. Availability could be made upon request to the lead contact after execution of a data transfer agreement with GR.

Code Availability. The source code of the bulk RNA-seq data, Visium data, and CosMx data analyses is available on GitHub (https://github.com/AhmedAmineAnzali/MGC_Paper_Analysis). The source code of the AI platform is available on GitHub (https://github.com/mgc-ai-cancer-discovery/mgc-ai-cancer-discovery). All methods and software packages used in the study have been documented and explained in ways accessible to the broader scientific audience.

Further information and requests for resources and code should be directed to and will be fulfilled by the corresponding author.

Authors’ Disclosures

G. Gessain reports grants from Institut National du Cancer—PRT-K 2022 and Prix Fonds Recherche 2021 de la Société Française de Pathologie during the conduct of the study; in addition, G. Gessain has a patent EP24305278.4 pending. M. Lerousseau reports other support from Spotlight Medical outside the submitted work; in addition, M. Lerousseau has a patent EP24305278.4 pending to Gustave Roussy. A. Auperin reports grants from Government: PRT-K 2022 during the conduct of the study; other support from MerckSD outside the submitted work. S. Uderhardt reports grants from Deutsche Forschungsgesellschaft DFG during the conduct of the study. F. Ginhoux reports a patent for Products and Uses Thereof for Predicting the Sensitivity of a Subject to Cancer Immunotherapy pending. No disclosures were reported by the other authors.

Authors' Contributions

G. Gessain: Conceptualization, resources, data curation, software, formal analysis, supervision, funding acquisition, validation, investigation, visualization, methodology, writing–original draft, project administration, writing–review and editing. **A.-A. Anzali:** Data curation, formal analysis, methodology, writing–review and editing. **M. Lerousseau:** Software, formal analysis, investigation, methodology, writing–review and editing. **K. Mulder:** Software, formal analysis, investigation, methodology, writing–review and editing. **M. Bied:** Formal analysis, investigation. **A. Auperin:** Formal analysis, funding acquisition, investigation, methodology, writing–review and editing. **D. Stockholm:** Formal analysis, investigation, methodology. **N. Signolle:** Formal analysis. **F. Sassi:** Data curation, formal analysis. **M.E. Marques Da Costa:** Resources, data curation. **A. Marchais:** Resources, data curation. **A. Sayadi:** Formal analysis. **D. Weidner:** Formal analysis. **S. Uderhardt:** Formal analysis. **Q. Blampey:** Formal analysis, methodology. **S.R. Nakkireddy:** Formal analysis, methodology. **S. Broutin:** Resources. **C.-A. Dutertre:** Formal analysis. **P. Busson:** Resources. **T. Walter:** Funding acquisition, methodology. **A. Marhic:** Resources. **A. Moya-Plana:** Resources. **J. Guerlain:** Resources. **I. Breuskin:** Conceptualization, resources, project administration. **O. Casiraghi:** Conceptualization, resources, project administration. **P. Gorphe:** Conceptualization, resources, funding acquisition, project administration, writing–review and editing. **M. Classe:** Conceptualization, resources, project administration. **J.-Y. Scoazec:** Conceptualization, resources, funding acquisition, writing–review and editing. **C. Bleriot:** Conceptualization, resources, formal analysis, supervision, investigation, project administration, writing–review and editing. **F. Ginhoux:** Conceptualization, resources, supervision, funding acquisition, investigation, methodology, project administration, writing–review and editing.

Acknowledgments

G. Gessain was supported by the grant "Année-Recherche en Médecine", the grant for DUERTECC ("Diplôme Universitaire Européen de Recherche Translationnelle Et Clinique en Cancérologie") and the "Prix Fonds Recherche 2021 de la Société Française de Pathologie". S. Uderhardt is supported by DFG (project-IDs 448121430, 405969122, 505539112), the Hightech Agenda Bavaria and by an ERC starting grant (project-ID 101039438). Volumetric tumor imaging was performed on a DFG-funded confocal microscope (project-ID 261193037). F. Ginhoux is supported by the Fondation Gustave Roussy and Fondation ARC—"Recruiting International Leaders 2020". This work was supported by the "Programme de Recherche Translationnelle en Cancérologie 2022 Institut National du Cancer PRT-K 2022". T. Walter received funding from ITMO Cancer (20CM107-00).

Note

Supplementary data for this article are available at Cancer Discovery Online (http://cancerdiscovery.aacrjournals.org/).

Received January 5, 2024; revised July 1, 2024; accepted September 12, 2024; published first September 16, 2024.

REFERENCES

1. Sung H, Ferlay J, Siegel RL, Laversanne M, Soerjomataram I, Jemal A, et al. Global cancer statistics 2020: GLOBOCAN estimates of incidence and mortality worldwide for 36 cancers in 185 countries. CA Cancer J Clin 2021;71:209–49.
2. Ferris RL, Blumenschein G Jr, Fayette J, Guigay J, Colevas AD, Licitra L, et al. Nivolumab for recurrent squamous-cell carcinoma of the head and neck. N Engl J Med 2016;375:1856–67.
3. Johnson DE, Burtness B, Leemans CR, Lui VWY, Bauman JE, Grandis JR. Head and neck squamous cell carcinoma. Nat Rev Dis Primers 2020;6:92.
4. Hanahan D. Hallmarks of cancer: new dimensions. Cancer Discov 2022;12:31–46.
5. Pittet MJ, Michielin O, Migliorini D. Clinical relevance of tumour-associated macrophages. Nat Rev Clin Oncol 2022;19:402–21.
6. Mulder K, Patel AA, Kong WT, Piot C, Halitzki E, Dunsmore G, et al. Cross-tissue single-cell landscape of human monocytes and macrophages in health and disease. Immunity 2021;54:1883–900.e5.
7. Colonna M. The biology of TREM receptors. Nat Rev Immunol 2023;23:580–94.
8. Molgora M, Liu YA, Colonna M, Cella M. TREM2: a new player in the tumor microenvironment. Semin Immunol 2023;67:101739.
9. Burkhardt A, Gebbers JO. Giant cell stromal reaction in squamous cell carcinomata. Electronmicroscopic and ultrahistochemical observations on the genesis and functional activity of multinucleated giant cells in bleomycin-induced tumor regression. Virchows Arch A Path Anat Histol 1977;375:263–80.
10. Patil S, Rao RS, Ganavi BS. A foreigner in squamous cell carcinoma. J Int Oral Heal 2013;5:147–50.
11. Wang H, Zhou J, Li J, Geng Y, Meng P, Ma C, et al. A study of multinucleated giant cells in esophageal cancer. Clin Immunol 2021;222:108600.
12. de Medeiros VA, de Pontes Santos HB, de Brito Monteiro BV, da Paz AR, Alves PM, Nonaka CFW. Absence of multinucleated giant cell reaction as an indicator of tumor progression in oral tongue squamous cell carcinoma. Eur Arch Otorhinolaryngol 2022;279:3123–30.
13. Pandiar D, Ramani P, Krishnan RP, Monica K. Multifaceted multinucleated giant cells in oral squamous cell carcinoma. Oral Oncol 2021;121:105400.
14. Marhic A, Guerlain J, Benmoussa N, Breuskin I, Honart J-F, Janot F, et al. Replacement of lip-split mandibulotomy by pull-through approach for T3–4 oral carcinomas. Int J Oral Maxillofac Surg 2021;50:1123–30.
15. Moya-Plana A, Aupérin A, Guerlain J, Gorphe P, Casiraghi O, Mamelle G, et al. Sentinel node biopsy in early oral squamous cell carcinomas: long-term follow-up and nodal failure analysis. Oral Oncol 2018;82:187–94.
16. Bill R, Wirapati P, Messemaker M, Roh W, Zitti B, Duval F, et al. CXCL9:SPP1 macrophage polarity identifies a network of cellular programs that control human cancers. Science 2023;381:515–24.
17. Carnicer-Lombarte A, Chen ST, Malliaras GG, Barone DG. Foreign body reaction to implanted biomaterials and its impact in nerve neuroprosthetics. Front Bioeng Biotechnol 2021;9:622524.
18. Safall H, Azar HA. Keratin granulomas in irradiated squamous cell carcinoma of various sites. Cancer Res 1966;26:500–8.
19. Braun OM, Neumeister B, Popp W, Scherrer R, Dobrowsky E, Dobrowsky W, et al. Histologic tumor regression grades in squamous cell carcinoma of the head and neck after preoperative radiochemotherapy. Cancer 1989;63:1097–100.
20. Chen W, Zhao L, Agoston A, White A, Mazzola E, Boyle PJ, et al. Florid foreign body-type giant cell response to keratin is associated with improved overall survival in patients receiving preoperative therapy for esophageal squamous cell carcinoma. Am J Surg Pathol 2021;45:1648–60.
21. Molgora M, Esaulova E, Vermi W, Hou J, Chen Y, Luo J, et al. TREM2 modulation remodels the tumor myeloid landscape enhancing anti-PD-1 immunotherapy. Cell 2020;182:886–900.e17.
22. Yofe I, Shami T, Cohen N, Landsberger T, Sheban F, Stoler-Barak L, et al. Spatial and temporal mapping of breast cancer lung metastases identify TREM2 macrophages as regulators of the metastatic boundary. Cancer Discov 2023;13:2610–31.
23. Timperi E, Gueguen P, Molgora M, Magagna I, Kieffer Y, Lopez-Lastra S, et al. Lipid-associated macrophages are induced by cancer-associated fibroblasts and mediate immune suppression in breast cancer. Cancer Res 2022;82:3291–306.
24. Maynard A, McCoach CE, Rotow JK, Harris L, Haderk F, Kerr DL, et al. Therapy-induced evolution of human lung cancer revealed by single-cell RNA sequencing. Cell 2020;182:1232–51.

25. Xiong D, Wang Y, You M. A gene expression signature of TREM2^{hi} macrophages and γδ T cells predicts immunotherapy response. Nat Commun 2020;11:5084.
26. Binnewies M, Pollack JL, Rudolph J, Dash S, Abushawish M, Lee T, et al. Targeting TREM2 on tumor-associated macrophages enhances immunotherapy. Cell Rep 2021;37:109844.
27. Drobin K, Marczyk M, Halle M, Danielsson D, Papiez A, Sangsuwan T, et al. Molecular profiling for predictors of radiosensitivity in patients with breast or head-and-neck cancer. Cancers (Basel) 2020;12:753.
28. Liu Z, Zhang Y, Ma N, Yang Y, Ma Y, Wang F, et al. Progenitor-like exhausted SPRY1$^+$CD8$^+$ T cells potentiate responsiveness to neoadjuvant PD-1 blockade in esophageal squamous cell carcinoma. Cancer Cell 2023;41:1852–70.e9.
29. Almangush A, Bello IO, Heikkinen I, Hagström J, Haglund C, Kowalski LP, et al. Stromal categorization in early oral tongue cancer. Virchows Arch 2021;478:925–32.
30. Heikkinen I, Bello IO, Wahab A, Hagström J, Haglund C, Coletta RD, et al. Assessment of tumor-infiltrating lymphocytes predicts the behavior of early-stage oral tongue cancer. Am J Surg Pathol 2019;43:1392–6.
31. Franken A, Bila M, Mechels A, Kint S, Van Dessel J, Pomella V, et al. CD4$^+$ T cell activation distinguishes response to anti-PD-L1+anti-CTLA4 therapy from anti-PD-L1 monotherapy. Immunity 2024;57:541–58.e7.
32. Wu J, Zhang T, Xiong H, Zeng L, Wang Z, Peng Y, et al. Tumor-infiltrating CD4$^+$ central memory T cells correlated with favorable prognosis in oral squamous cell carcinoma. J Inflamm Res 2022;15:141–52.
33. Berbís MA, McClintock DS, Bychkov A, Van der Laak J, Pantanowitz L, Lennerz JK, et al. Computational pathology in 2030: a Delphi study forecasting the role of AI in pathology within the next decade. EBioMedicine 2023;88:104427.
34. van der Laak J, Litjens G, Ciompi F. Deep learning in histopathology: the path to the clinic. Nat Med 2021;27:775–84.
35. Bankhead P, Loughrey MB, Fernández JA, Dombrowski Y, McArt DG, Dunne PD, et al. QuPath: open source software for digital pathology image analysis. Sci Rep 2017;7:16878.
36. Hendry S, Salgado R, Gevaert T, Russell PA, John T, Thapa B, et al. Assessing tumor-infiltrating lymphocytes in solid tumors: a practical review for pathologists and proposal for a standardized method from the international immunooncology biomarkers working group: part 1: assessing the host immune response, TILs in invasive breast carcinoma and ductal carcinoma in situ, metastatic tumor deposits and areas for further research. Adv Anat Pathol 2017;24:235–51.
37. Broders AC. Squamous cell epithelioma of the lip. A study of five hundred and thirty-seven cases. JAMA 1920;74:656–64.
38. Tian Z, Shen C, Chen H, He T. FCOS: Fully convolutional one-stage object detection. In: 2019 IEEE/CVF International Conference on Computer Vision (ICCV); 2019 Oct 27–Nov 2; Seoul, South Korea: IEEE; 2019. p. 9626–35.
39. He K, Zhang X, Ren S, Sun J. Deep residual learning for image recognition kaiming. In: 2016 IEEE Conference on Computer Vision and Pattern Recognition (CVPR); 2016 Jun 27–30; Las Vegas, NV: IEEE; 2016. p. 770–8.
40. Deng J, Dong W, Socher R, Li L-J, Li K, Fei-Fei L. ImageNet: a large-scale hierarchical image database. In: 2009 IEEE Conference on Computer Vision and Pattern Recognition; 2009 Jun 20–25; Miami, FL: IEEE; 2009. p. 248–55.
41. Buslaev A, Iglovikov VI, Khvedchenya E, Parinov A, Druzhinin M, Kalinin AA. Albumentations: fast and flexible image augmentations. Information 2020;11:125.
42. Kingma DP, Ba JL. Adam: a method for stochastic optimization. In: 3rd International Conference on Learning Representations, ICLR 2015; 2015 May 7–9; San Diego, CA: ICLR; 2015.
43. Lin T-Y, Goyal P, Girshick R, He K, Dollar P. Focal loss for dense object detection. Proceedings of the IEEE International Conference on Computer Vision; 2017 Oct 22–29; Venice, Italy: IEEE; 2017. p. 2999–3007.
44. Paszke A, Gross S, Massa F, Lerer A, Bradbury Google J, Chanan G, et al. PyTorch: an imperative style, high-performance deep learning library. In: Advances in Neural Information Processing Systems. NeurIPS. Curran Associates, Inc; 2019. p. 8026–37.
45. Heberle H, Meirelles GV, da Silva FR, Telles GP, Minghim R. InteractiVenn: a web-based tool for the analysis of sets through venn diagrams. BMC Bioinformatics 2015;16:169.
46. Blampey Q, Mulder K, Gardet M, Christodoulidis S, Dutertre C-A, André F, et al. Sopa: a technology-invariant pipeline for analyses of image-based spatial omics. Nat Commun 2024;15:4981.
47. Palla G, Spitzer H, Klein M, Fischer D, Schaar AC, Kuemmerle LB, et al. Squidpy: a scalable framework for spatial omics analysis. Nat Methods 2022;19:171–8.
48. Liu J, Lichtenberg T, Hoadley KA, Poisson LM, Lazar AJ, Cherniack AD, et al. An integrated TCGA pan-cancer clinical data resource to drive high-quality survival outcome analytics. Cell 2018;173:400–16.e11.